Creating Ligand-Free Silicon Germanium Alloy Nanocrystal Inks

Folarin Erogbogbo,[⊥] Tianhang Liu,[†,⊥,∥] Nithin Ramadurai,[‡] Phillip Tuccarione,[‡] Larry Lai,[⊥] Mark T. Swihart,[‡,*] and Paras N. Prasad[§,⊥,∥,*]

[†]School of Science, Changchun University of Science and Technology, Changchun, 130022, Jilin, China, [‡]Department of Chemical and Biological Engineering, [§]Department of Chemistry and [⊥]Institute for Lasers, and Photonics and Biophotonics, The University at Buffalo, State University of New York, Buffalo, New York 14260-4200, United States, and [∥]International Joint Research Center for Nanophotonics and Biophotonics, Changchun, 130022, Jilin, China

ABSTRACT Particle size is widely used to tune the electronic, optical, and catalytic properties of semiconductor nanocrystals. This contrasts with bulk semiconductors, where properties are tuned based on composition, either through doping or through band gap engineering of alloys. Ideally, one would like to control both size and composition of semiconductor nanocrystals. Here, we demonstrate production of silicon–germanium alloy nanoparticles by laser pyrolysis of silane and germane. We have used FTIR, TEM, XRD, EDX, SEM, and TOF-SIMS to conclusively determine their structure and composition. Moreover, we show that upon extended sonication in selected solvents, these bare nanocrystals can be stably dispersed without ligands, thereby providing the possibility of using them as an ink to make patterned films, free of organic surfactants, for device fabrication. The engineering of these SiGe alloy inks is an important step toward the low-cost fabrication of group IV nanocrystal optoelectronic, thermoelectric, and photovoltaic devices.

KEYWORDS: silicon · germanium · nanoparticles · alloy nanoparticles · aerosol

Over the past few decades, semiconductor nanoparticles have generated great interest[1,2] due to their size-tunable optical and electronic properties that have led to applications in electronics,[3] optoelectronics,[4] photovoltaics,[5] photocatalysis,[6] and bioimaging.[7,8] However, some applications require multiple characteristics in a single nanoparticle system. Very small nanoparticles may be desired for *in vivo* imaging,[8,9] in order to achieve a range of different emission colors.[10] Size is an important factor when nanoparticles are incorporated into larger superstructures like mesoporous materials in photovoltaics.[11,12] Thus, controlling the size and size distribution of the nanoparticles is of utmost importance. However, with the advent of optimized methods of nanoparticle synthesis, controlling the size distribution of single-component nanoparticles is no longer a major concern for colloidally synthesized materials such as CdSe quantum dots. Some interest has thus shifted to modifying the composition in the view of improving the properties of the nanoparticles. Intentional doping, with impurities, is a critical method used in modifying the properties of bulk semiconductors.[13,14] Usually, the intentional doping with impurity atoms only slightly changes the composition, but the electrical, optical, and magnetic properties may be changed significantly.[15] Doping usually employs elements of different electronic valency than the material being doped, which introduces additional electrons or empty states (holes) into the electronic structure of the material. Doping of nanoparticles can be exceedingly difficult, because a small number of dopant atoms per particle may correspond to a very high doping level, in comparison to doping levels used in bulk semiconductors.[15]

Alloying involves significantly varying the composition of the nanoparticles to change their properties. In contrast to doping, alloying involves mixing materials of the same electronic valency, to smoothly vary the properties from those of one material to another. This provides an additional degree of freedom to the material design (*i.e.*, selecting desirable properties) of the nanoparticles.[16] Alloy nanoparticles can be used to meet multiple requirements of nanoparticle size and properties. Because the optical and physical properties of the alloy nanoparticles vary with composition, these properties can be tuned by modifying composition while maintaining a small size.

Challenges are also faced in alloy nanoparticle research, as it requires new methods of synthesis to produce the desired structures. To obtain homogeneous alloys, the growth rates of the two or more constituent materials must be comparable and the conditions necessary for the growth of one constituent material must not impede the growth of the other constituent material(s).[17,18] Also, the structure and bonding characteristics of the constituent materials must be very similar to facilitate smooth mixing.[16] Processes and conditions must therefore be identified

* Address correspondence to pnprasad@buffalo.edu, swihart@buffalo.edu.

Received for review June 23, 2011 and accepted September 19, 2011.

Published online September 19, 2011
10.1021/nn2023304

for which both kinetic and thermodynamic considerations (*i.e.*, the phase diagram) favor alloy formation.

Interest in alloying group (IV) semiconductors, namely, silicon and germanium, is rapidly growing. Germanium has mostly been ignored as a microelectronics material since its use in 1947 to build the first transistor,[19] but is experiencing somewhat of a revival due to its potential in high-speed and opto-electronic Si–Ge heterostructures.[20,21] The electron mobility of germanium is twice that of silicon,[22] and it has a higher optical absorption coefficient than silicon.[23] Germanium also has a smaller band gap than silicon (for Ge: at $T = 300$ K, $E_g = 0.66$ eV and at $T = 0$ K, $E_g = 0.741$ eV; for Si: at $T = 300$ K, $E_g = 1.12$ eV and at $T = 0$ K, $E_g = 1.16$ eV).[24] However, germanium lacks a stable oxide, and this has been a major disadvantage relative to silicon in microelectronics, where thermally grown silicon dioxide was the dominant dielectric material for several decades. For applications in photovoltaics and photodetection, alloys of silicon and germanium can be designed to absorb a large range of the solar spectrum by varying the composition. This process is also known as "band gap engineering" or "band-structure engineering".[25,26] By varying the alloy composition, the band gap of bulk $Si_{1-x}Ge_x$ can be varied between 0.66 and 1.12 eV. Higher band gaps can be achieved *via* quantum confinement in small nanocrystals. Thus, the band gap of $Si_{1-x}Ge_x$ nanocrystals can potentially be tuned across the entire visible and near-IR spectrum.

To date, the most studied mode of synthesis of silicon–germanium alloy nanoparticles has been *via* solid-phase nucleation and growth at high temperatures. These methods produce nanoparticles embedded in a silicon oxide matrix. The process involves co-sputtering of germanium, silicon, and silicon dioxide targets onto a silicon substrate and then annealing (at over 1100 °C)[27] or rapid thermal annealing (at 900 °C) in an inert atmosphere.[28,29] Silicon–germanium alloys have also been synthesized by thermal evaporation of powders of silicon and germanium on a glass substrate at temperatures greater than 1400 °C[30,31] and by using molecular beam epitaxy, to grow silicon–germanium alloy nanoparticles on a silicon substrate.[32,33] In most cases, the matrix material passivates the nanoparticle surfaces well, but the range of possible surface treatments for the embedded nanoparticles and the flexibility of using embedded nanoparticles for device applications are very limited.[34] Liquid-phase silicon–germanium alloy nanoparticle synthesis techniques[35,36] are convenient for subsequent liquid-phase surface-functionalization reactions, but techniques are usually very time-consuming, have low material yields, and produce a broad range of sizes and shapes. Recently, Pi *et al.*[37] developed a method to produce free-standing silicon germanium alloy nanocrystals (adapted from their technique to produce free-standing silicon nanocrystals[38] and germanium nanocrystals[34]) by nonthermal plasma decomposition of silane and germane. However, a drawback of this technique was the difficulty in producing macroscopic quantities of the nanoparticles.

Here, we present the synthesis of free-standing silicon–germanium alloy nanoparticles by laser-induced simultaneous pyrolysis of silane and germane in an aerosol reactor. Despite many reports of silicon nanoparticle synthesis by laser pyrolysis, dating back to 1982,[39,40] this method has not previously been used to produce germanium nanoparticles. The only prior report of $Si_{1-x}Ge_x$ production by laser pyrolysis used a pulsed laser and focused on a single silicon-rich composition ($Si_{0.92}Ge_{0.08}$).[41] Production of $Si_{1-x}Ge_x$ alloys by laser pyrolysis or other thermal methods is made challenging by the difference in reactivity between silicon precursor compounds (typically silane or disilane) and the corresponding germanium precursor compounds (*e.g.*, germane). The less thermally stable germane tends to decompose first and nucleate germanium particles before silane significantly decomposes, leading to separate populations of relatively large germanium-rich particles and smaller silicon-rich particles. We overcome this challenge by using the silane itself as the photosensitizer for laser pyrolysis, so that thermal decomposition is preferentially initiated where silane concentration is highest, and by configuring the optics and flows to achieve very high heating rate in a small reactor volume. This minimizes the delay between the onset of germane decomposition and silane decomposition. The pulsed laser pyrolysis approach achieves a similar effect at the expense of low production rates that result from the low duty cycle of the pulsed laser.

In this work, we also show that the bare Si, Ge, and $Si_{1-x}Ge_x$ nanoparticles can form colloidally stable dispersions in organic solvents such as benzonitrile, similar to the result recently reported by Kortshagen and Holman.[42] However, while they observed the formation of stable dispersions only for germanium particles with mixed chlorine–hydrogen surface termination, the particles prepared in our work are free of chlorine.

RESULTS AND DISCUSSION

The atomic fractions of germanium (x) in the silicon–germanium nanocrystals ($Si_{1-x}Ge_x$) were determined from SEM-EDS analysis of the bulk nanoparticle powder. The different ratios of flow rates of germane: silane used were 1:22, 1:11, 1:9, and 1:1.7, and the corresponding germanium atomic fractions in the product powders were $x =$ 0.31, 0.56, 0.64, and 0.96. All powders were substantially enriched in germanium relative to the germane:silane ratio supplied to the reactor. This is to be expected, given the much lower thermal stability of germane relative to silane. Figure 2a shows the EDS spectra of the four different samples. SEM-EDS analysis of a single nanoparticle on a TEM grid

(Figure 2b) showed that they were indeed an alloy of silicon and germanium rather than a mixture of separate silicon and germanium nanoparticles. The particles were observed in clusters of a few nanoparticles, as depicted in Figure 2b. Individual particles within these clusters were analyzed. While some variation from particle to particle was observed, the average values were close to the values measured for the bulk sample.

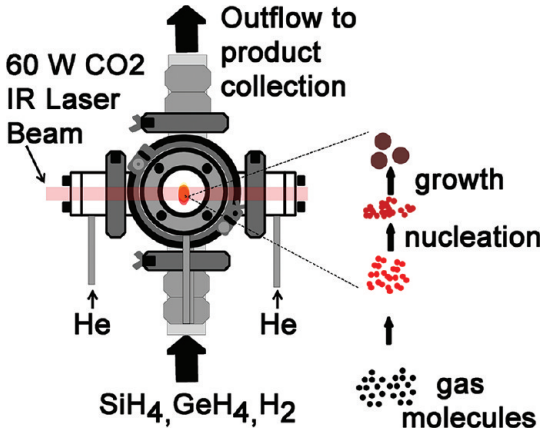

Figure 1. Schematic of the aerosol reactor with the points of gas inlet.

The powder XRD pattern of silicon[37] is characterized by three peaks at 2θ values (for Cu Kα X-rays) of about 28.7, 47.4, and 56.3 degrees, which correspond to diffraction from the Si(111), (220), and (311) lattice planes, respectively. The corresponding peaks in the XRD pattern of germanium are at 27.4, 45.6, and 53.8 degrees, respectively. Figure 2c shows that all of the XRD peaks shift from positions close to those of silicon toward those for germanium as the atomic fraction of germanium in the alloy nanoparticles increases. Upon close observation, a secondary peak or shoulder can be observed in the XRD plots for intermediate compositions. These XRD traces were fit to a mixture of two subpopulations of particles of different composition, using MAUD version 2.32.[43] In this fitting procedure, the amount, lattice constant, and size of the two particle subpopulations were varied independently. The composition of each subpopulation was estimated by applying Vegard's law to the fitted lattice constant. Results of this analysis are shown in Figure 2d. The lattice constants for the different germanium compositions were between 5.45 and 5.67 Å. Figures S1–S4 show the fits of the XRD traces from this analysis. The lattice constant for bulk silicon and bulk germanium are 5.43 and 5.66 Å, respectively.[31,44] Our pure silicon

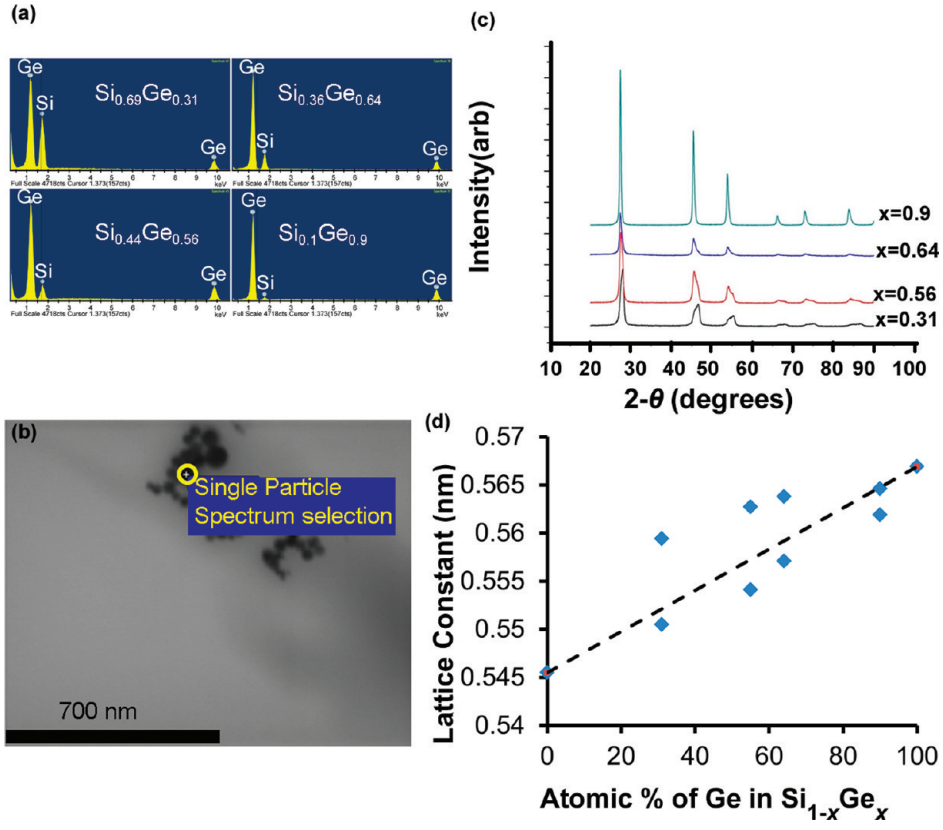

Figure 2. (a) Broad area EDS spectra of samples of four different compositions, (b) SEM image showing a typical region used for single-particle EDS analysis, (c) XRD powder patterns from the silicon–germanium alloy nanoparticles (*x* in the plot represents the atomic fraction of germanium in the nanoparticles, as measured by EDS), and (d) lattice constants of $Si_{1-x}Ge_x$ nanoparticles obtained from XRD analysis as a function of germanium content. Two lattice constants for two subpopulations of particles were determined as described in the text.

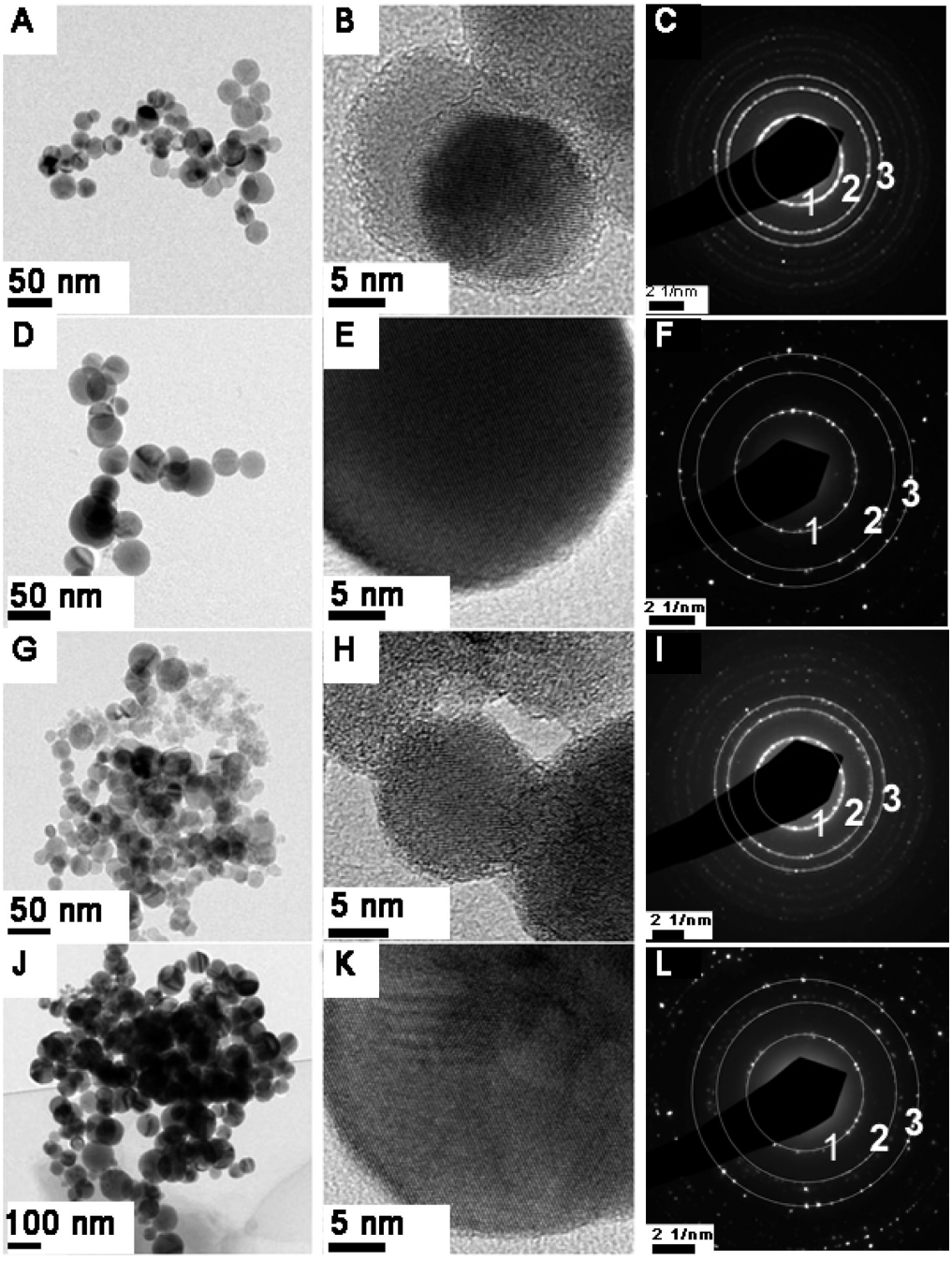

Figure 3. TEM images of the silicon−germanium alloy nanoparticles on a carbon grid, with an atomic fraction of germanium of (a−c) 0.31, (d−f) 0.56, (g−i) 0.64, and (j−l) 0.9, respectively, examined under (a,d,g,j) low magnification and (b,e,h,k) high magnification, and corresponding selected area electron diffraction patterns (c,f,i,l).

and germanium nanoparticles had measured lattice constants of 5.456 and 5.673 Å, and these latter values were used in estimating the compositions from Vegard's law. For the sample with $x = 0.31$, this analysis gave 49.7 wt % $Si_{0.77}Ge_{0.23}$ and 50.3 wt % $Si_{0.36}Ge_{0.64}$; for $x = 0.56$, it gave 46 wt % $Si_{0.61}Ge_{0.39}$ and 54 wt % $Si_{0.21}Ge_{0.79}$; for $x = 0.64$, it gave 56 wt % $Si_{0.47}Ge_{0.53}$ and 44 wt % $Si_{0.16}Ge_{0.84}$; and for $x = 0.96$ it gave 28.5 wt % $Si_{0.25}Ge_{0.75}$ and 72 wt % $Si_{0.12}Ge_{0.88}$. The corresponding overall compositions were 40, 58, 65, and 83 at. % Ge for the four samples, which is in reasonable agreement with the EDS measurements, given the significant uncertainties in both methods.

Transmission electron microscopy images of the silicon−germanium alloy nanoparticles of varying composition are shown in Figure 3. Particles range from 15 to 30 nm in diameter and are all near spherical in shape. The lattice fringes seen in the individual nanoparticles (b,e,h,k), and the selected area diffraction patterns (c,f,i,l), demonstrate the crystallinity of the nanoparticles. Figures S5 and S6 show TEM images of silicon and germanium nanoparticles, respectively.

Diffraction rings corresponding to the 111, 220, and 311 planes are highlighted as circles in the images. Both measurements of lattice fringes in HRTEM images and SAED ring diameters showed an overall trend of increasing lattice constant with increasing germanium content. However, because XRD provides much more precise measurement of lattice parameters, we relied on the XRD patterns for quantitative analysis of lattice constants as described above. Figure S7 shows TEM images of alloy nanoparticles that exhibit different crystal orientations in the same particle, separated by twinning defects.[45]

In FTIR spectroscopy, the bond stretching absorption of surface Si−H and Ge−H appear in the 1800−2300 cm^{-1} region, and the bond-bending absorption of surface Si−H and Ge−H appear in the 500−1100 cm^{-1} region. These peaks are expected to shift with composition. Thus, particles were briefly etched to achieve H-termination of their surface, and their FTIR spectra were examined. The hydride peaks of freshly

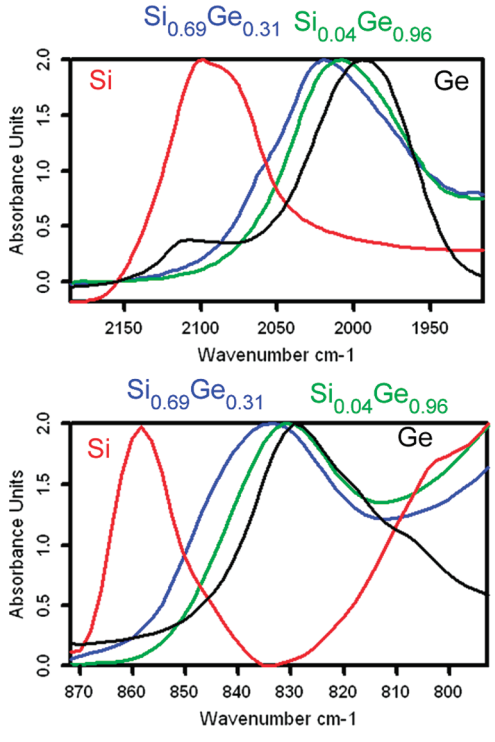

Figure 4. FTIR spectra of Si−H, SiGe−H, and Ge−H with maximum peaks in the (a) 1950 to 2150 cm^{-1} range and (b) 800−870 cm^{-1} range.

(HF/HNO_3)-etched silicon, silicon−germanium alloy, and germanium nanoparticles were evaluated immediately after treatment. Figure 4a displays the peaks with maxima between 1950 and 2150 cm^{-1}, which are attributed to Si−H stretching modes and Ge−H stretching modes. The silicon hydride absorption peak appears at 2099 cm^{-1}, while the germanium hydride absorption peak appears at 1994 cm^{-1}. The absorbance peaks of the silicon germanium alloy nanoparticles appear between the Si and Ge nanoparticle individual peaks at 2008 and 2019 cm^{-1}. We note that the peaks lie closer to the positions characteristic of Ge−H than those of Si−H. Figure 4b shows the Si−H rocking mode with a peak at 858 cm^{-1}. This peak also shifts toward a Ge−H peak at 829 cm^{-1} as the concentration of Ge increases, and the SiGe peaks are located at 830 and 834 cm^{-1}. The full spectra for these particles are given in the Supporting Information (Figures S8−S11). The fact that these IR absorption peaks are closer to the positions of the pure Ge peaks than would be predicted based upon their overall stoichiometry suggests the possibility of slight Ge surface segregation in the particles. However, no quantitative conclusions can be drawn from these measurements alone.

The results from the TOF-SIMS analysis of the silicon−germanium alloy nanoparticles are presented in Table 1, which gives the atomic fraction of total germanium with respect to the total amount of germanium and silicon present (total count). The atomic fractions of GeH and GeOH (relative to total GeH + SiH and GeOH + SiOH) in the sample are also shown in the table. For these nanoparticles in the size range 10−25 nm, the ion beam is expected to fully ablate complete particles. Hence, the TOF-SIMS composition measurements are characteristic of the entire sample and not just the particle surfaces. Figures S12−S15 show the TOF-SIMS mass spectra for the nanoparticles. Figure 5 compares the atomic fractions obtained from the XRD/Vegard's law analysis and from the EDS measurements to those from the TOF-SIMS analysis. The TOF-SIMS results are in reasonable agreement with the EDS measurements and in near-perfect agreement with the results of the Vegard's law analysis of fitted XRD patterns. The atomic fractions of GeH in comparison to the total SiH and GeH were lower than the overall Ge atomic fraction, suggesting that hydrogen is preferentially bonded to silicon. The opposite was true

TABLE 1. Results of the TOF-SIMS Analysis of Different Alloy Samples As a Function of Flow Rate

ratio of initial reactant flow rates (silane:germane)	atomic fraction of Ge *Ge/(Si+Ge)*	atomic fraction of GeH *GeH/(SiH+GeH)*	atomic fraction of GeOH *GeOH/(SiOH/GeOH)*
1:22	0.4	0.3	0.51
1:11	0.58	0.47	0.68
1:9	0.65	0.55	0.84
1:1.7	0.86	0.68	0.95

for the atomic fraction of GeOH relative to the total count for SiOH and GeOH, indicating a higher likelihood of finding hydroxide-terminated Ge than Si.

Figure 6a shows the absorbance spectra of unfiltered Si, Ge, and SiGe nanoparticles at the same concentration. The Si and SiGe samples were measured in methanol, while the Ge sample was measured in water. There is a clear red shift of absorbance from silicon to silicon−germanium nanoparticles, reflecting a change in band gap due to the formation of an alloy. A substantial fraction of Ge nanoparticles dispersed in water could pass through a filter of 200 nm nominal pore size (50% recovery). A smaller fraction of Si and $Si_{0.69}Ge_{0.31}$ nanoparticles dispersed in methanol could pass through such a filter (<20% recovery). The absorbance of germanium in water before and after filtration is depicted in Figure 6b. Comparing the absorbance at 600 nm after filtration indicates that slightly over 50% of the particles were recovered. However, quantitative analysis of the extinction spectra is complicated by scattering from aggregated particles in the unfiltered dispersion. The Si and $Si_{0.69}Ge_{0.31}$ nanoparticles were somewhat dispersible in methanol. However, water and methanol are not the most suitable solvents for use in fabrication of optoelectronic or photovoltaic devices. Thus, silicon and germanium nanoparticles are often modified with surface ligands that allow them to be stably dispersed in nonpolar organic solvents. Shorter ligands are normally more desirable to promote electron mobility in the final device, after solvent removal; however, shorter ligands are less effective in stabilizing the nanoparticle dispersions.

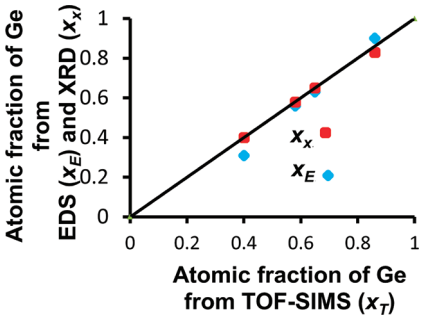

Figure 5. Plot of atomic fraction of germanium obtained from EDS measurements and from fitting of XRD spectra *vs* atomic fraction of germanium obtained from TOF-SIMS measurements. The solid line would result from perfect agreement between methods.

Holman and Korshagen[42] recently showed that ligand-free germanium nanoparticles can be stably dispersed in benzonitrile and some other solvents that may be useful for producing nanocrystal-based optoelectronic and photovoltaic devices. The dispersibility of their particles was attributed to electrostatic stabilization that stemmed from partial chlorine termination of their nanoparticle surfaces. Surprisingly, we found that our Ge nanoparticles, which are free of halide termination, were also dispersible in benzonitrile after sufficient sonication. About 5% of the particles went through a 200 nm filter after 10 min of sonication in a low-power ultrasonic bath. The absorbance of the filtered Ge particles in benzonitrile is shown in Figure 6c. In contrast, when Ge nanoparticles were sonicated for 10 min in acetonitrile, no detectable particles passed through the 200 nm filter (*i.e.*, the filtered dispersion looked identical to the pure solvent).

Our observation that a small fraction (∼5%) of the germanium nanoparticles were well dispersed in benzonitrile prompted us to extend the sonication time beyond what we would typically use to disperse nanoparticles and to revisit solvents in which no dispersibility was initially evident. Interestingly, particles that previously did not disperse in acetonitrile after 10 min of sonication passed through a 0.2 μm filter after 4 h of sonication in acetonitrile. The absorbance values of different concentrations of unfiltered and filtered samples are depicted in Figure 7a and c, respectively. The particle concentrations range from 0.006 to 0.09 mg/mL, and by integrating the area under the curve and assuming there is negligible scattering, 50−58% of the nanoparticles remained in the filtered dispersion. This unexpected increase in dispersibility is attributed to the

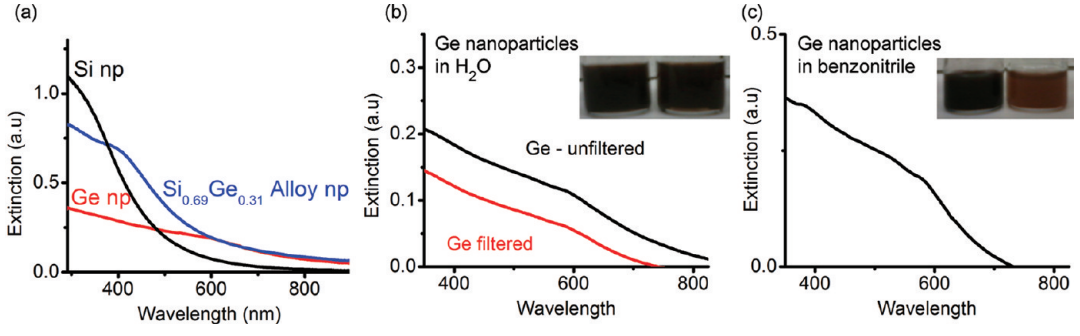

Figure 6. Extinction spectra of (a) silicon np and $Si_{0.69}Ge_{0.31}$ nanoparticles dispersed in methanol and Ge nanoparticles dispersed in water; (b) Ge nanoparticles in water before (black line) and after (red line) filtration through a filter with 200 nm nominal pore size. The inset includes an example of unfiltered (left) and filtered particles (right) dispersed in water. (c) Ge nanoparticles in benzonitrile filtered after 10 min sonication. The inset shows unfiltered (left) and filtered (right) Ge nanoparticles dispersed in benzonitrile.

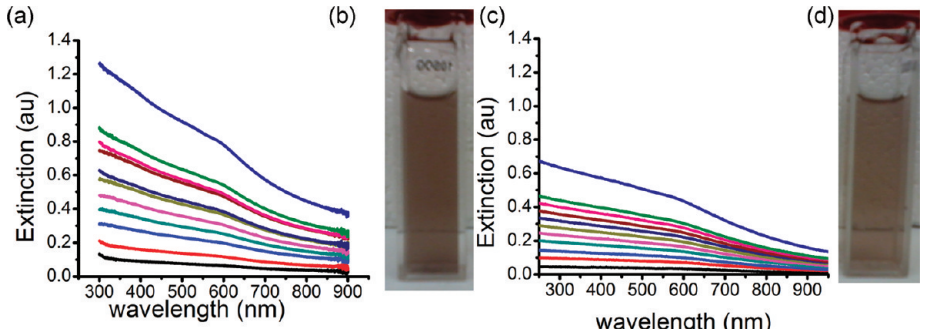

Figure 7. Extinction spectra of germanium nanoparticles dispersed in acetonitrile after 4 h of sonication (a, b) before and (c, d) after filtration.

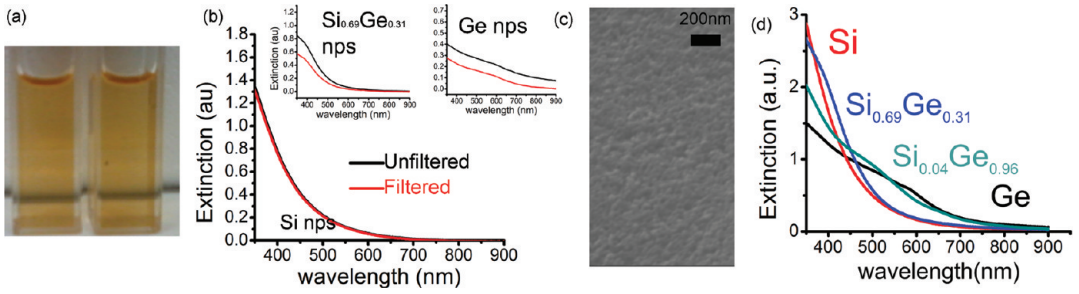

Figure 8. Nanoparticles in benzonitrile. (a) Photo of silicon nanoparticles unfiltered (left) and filtered (right) in benzonitrile. (b) Absorbance spectra of filtered and unfiltered silicon nanoparticles in benzonitrile. Left inset is absorbance spectra of $Si_{0.69}Ge_{0.31}$ nanparticles in benzonitrile, and right inset is Ge nanoparticles in benzonitrile. Black lines correspond to unfiltered nanoparticles. Red lines correspond to filtered nanoparticles. (c) SEM secondary electron image of the surface of a thin film formed by spin-coating silicon nanocrystals onto a glass slide and heating for 10 min at ~150 °C. (d) Absorbance spectra of filtered Si, $Si_{0.69}Ge_{0.31}$, $Si_{0.04}Ge_{0.96}$, and Ge nanoparticles.

slow breakup of the as-produced aggregated particles. If scattering is significant, the recovery values would be an underestimation; however, the size of the particles, the transparency of the colloidal solution (Figure 7b and d), and the brownish color of the colloidal solution suggest that scattering is negligible. Comparing unfiltered and filtered absorbance values of a 0.09 mg/mL solution of Ge at 600 nm, over 52% of the germanium nanoparticles formed a colloidal suspension in acetonitrile after 4 h of sonication, compared to the negligible amount observed when the nanoparticles were sonicated for 10 min in acetonitrile.

These surprising results prompted a reevaluation of samples that had no apparent nanoparticles in the filtrate. Si and $Si_{0.69}Ge_{0.31}$ nanoparticle samples previously had no observable suspension after 10 min of sonication and filtration in benzonitrile. After 4 h, however, colloidal suspensions were observed after filtration, indicating that this extended sonication is required for aggregates to break up (Figure S16). Extended sonication for 24 h allowed Si, $Si_{0.69}Ge_{0.31}$, and Ge nanoparticles to all form clear colloidal dispersions in benzonitrile. The absorbance spectra of filtered Si, Ge, and $Si_{0.69}Ge_{0.31}$ in benzonitrile are shown in Figure 8b. Evaluating the area under the filtered curve and unfiltered curves shows that ~100% of the silicon nanoparticles, about 64% of the $Si_{0.69}Ge_{0.31}$ nanoparticles, and about 51% of the Ge nanoparticles were retained after filtration. The absorbance spectrum and photographs of unfiltered and filtered Si nanoparticles are almost identical, as shown in Figure 8a and b. This result was also unexpected, as the motivation for evaluating the dispersibility of these particles was the observed dispersibility of Ge nanoparticles. Hence, we expected that Ge nanoparticles would be more dispersible. The smaller size of the Si nanoparticles (10−20 nm) may be a factor in their improved dispersibility compared to larger $Si_{0.69}Ge_{0.31}$ and Ge nanoparticles (15−30 nm). Spin-coating of these dispersed silicon nanoparticles gave a relatively smooth crack-free thin film, as shown in Figure 8c. TEM images show the particles have similar structure before (Figure S5) and after (Figure S17) the sonication process. The shapes and profiles of filtered samples are shown in Figure 8d. Even though there is not a clear symmetric peak, it is clear that the absorbance of the sample shifts toward the red as the composition of the alloys moves toward higher percentages of Ge.

DISCUSSION

This work may have important implications for photovoltaic and energy related research because (1) it shows that the silicon germanium alloys can be readily produced by laser pyrolysis, (2) it demonstrates that the simple method of extended sonication can provide colloidal dispersions of silicon, germanium,

and silicon germanium alloys in solvents compatible with device fabrication, and (3) smooth films can be formed from these colloidal solutions. A vast array of additional combinations of solvents, particles, and particle surface treatments remains to be explored, but these initial results are very promising. The solvents used here can also dissolve many polymers that may be mixed with the bare nanoparticles to produce inks for making nanocomposite coatings or patterns. This simple procedure may have been overlooked previously simply because dispersion of nanoparticles is expected to happen quickly, or not at all. Thus, extended low-intensity sonication should be further investigated as a tool for achieving colloidal stability of bare nanoparticles. No special ionic surface characteristics are needed.

CONCLUSION

Silicon–germanium alloy nanoparticles ($Si_{1-x}Ge_x$) have been synthesized by the simultaneous laser pyrolysis of silane and germane. Multiple characterization techniques indicate that the synthesized nanoparticles are indeed an alloy of silicon and germanium (as opposed to separate silicon and germanium nanocrystals). The atomic fraction of germanium in the different samples of the as-synthesized alloy nanoparticles was determined by both EDS and TOF-SIMS, and the results were consistent. The results from the XRD analysis (peak positions and lattice constants) further support the conclusion that the nanoparticles were an alloy of silicon and germanium and suggest that the overall sample may consist of subpopulations of relatively higher and lower Ge content. TEM imaging showed that the alloy nanoparticles are in the size range of 15 to 30 nm in diameter. The XRD data along with the TEM images and electron diffraction confirm that the synthesized nanoparticles are crystalline. Finally, we demonstrated that both the pure Si and Ge nanoparticles and the alloy nanoparticles can be dispersed in benzonitrile and acetonitrile using extended sonication in a conventional ultrasonic bath. This opens the door to forming stable, ligand-free inks of these group IV nanoparticles without the requirement of halogenated nanoparticle surfaces.

TABLE 2. Production Rates of $Si_{1-x}Ge_x$ at Different Flow Rate Ratios of Silane:Germane

flow rate of silane (sccm)	flow rate of germane (sccm)	approximate production rate (mg/h)
236	11	600
236	21	600
100	26	900
18	10	1500

EXPERIMENTAL METHODS

Synthesis of Nanoparticles. The silicon–germanium alloy nanoparticles were synthesized by laser-induced simultaneous pyrolysis of silane and germane, as shown schematically in Figure 1, similar to the method used to produce silicon nanoparticles, developed previously by our group.[46] A continuous laser beam (Coherent, model 42 laser emitting up to 60 W) was focused to a diameter of about 2 mm above the central reactant inlet. The reactant inlet consists of concentric tubes (inner tube o.d. = 1/8 in., outer tube o.d. = 3/8 in.). Silane, germane, and hydrogen enter through the inner tube, while pure hydrogen enters through the annular space between the tubes. Helium enters the reactor near the ends of the four horizontal arms of the six-way cross from which the reactor is constructed. Silane absorbs the laser energy at a wavelength of about 10.6 μm and is thereby heated. The flows of helium (passed through an oxygen trap to remove any traces of oxygen and water) and hydrogen (ultrapure carrier grade, 99.99%) confine the reactants to a region near the axis of the reactor, thus preventing the accumulation of the gases in the arms of the six-way cross of the reactor body. The exact dimensions of the reaction zone are difficult to determine, but can be estimated to be about 2 mm in diameter. Hydrogen also serves to increase the temperature at which the nanoparticles form and to decrease the growth rate of the particles (*i.e.*, control the rate of the reaction), since it is a byproduct of the particle formation process (*i.e.*, dissociation of silane and germane). All the gas flows to the reactor were controlled by mass flow controllers. The aerosol of particles formed in the reactor flows through cellulose nitrate membrane filters, where the particles are collected. The effluent gas stream from the collectors is passed through a furnace, where it is heated at 775 °C to decompose any residual silane and germane.

This method can produce silicon–germanium alloy nanoparticles at about 500–1500 mg/h in the present configuration. The particles are transferred from the sealed filter housings to airtight vials in a glovebox under nitrogen. Table 2 gives the production rates of $Si_{1-x}Ge_x$ for different flow rates of the reactants.

Etching of Si, SiGe, and Ge Nanoparticles. A 30 mg portion of the nanoparticle powder was dispersed in 3 mL of methanol with sonication. An 11 mL aliquot of an acid mixture containing HF (48 wt %) and HNO_3 (69 wt %) (10/1, v/v) was added to the resulting dispersion to initiate etching. The samples were etched for 30 s. The etching was slowed by adding about 20 mL of methanol. The particles were collected on a poly(vinylidene fluoride) membrane filter (nominal pore size 100 nm) and washed with excess methanol.

Characterization of Nanoparticles. UV–vis absorption spectra were acquired using a Shimadzu UV-3600 spectrophotometer. High-resolution transmission electron microscopy (HRTEM) images were obtained using a JEOL model JEM 2010 microscope at an acceleration voltage of 200 kV. The specimens were prepared by drop-coating the sample dispersion onto an amorphous carbon-coated 400 mesh copper grid, which was placed on filter paper to absorb excess solvent. Scanning electron microscopy (SEM) images were obtained using a Hitachi S4000 field emission microscope at an acceleration voltage of 25 kV. The bulk powders were placed on double-sided conductive carbon tapes (Ted Pella Inc.) for SEM-EDS analysis. Interference from carbon (from the tape) in the EDS analysis was avoided by placing sufficient nanoparticle powder on the surface to create a thickness of more than 2 mm. Energy dispersive X-ray spectroscopy (EDX/EDS) for elemental analysis was carried out in the SEM. A Rigaku Ultima IV X-ray diffractometer was used for X-ray diffraction studies. FTIR spectra were measured on a Bruker Vertex 70 spectrometer in attenuated total reflectance mode.

Time-of-Flight Secondary Ion Mass Spectrometry (TOF-SIMS). Samples were analyzed using a ToF-SIMS 5-100 instrument (IonTof Gmbh, Münster, Germany), equipped with a liquid metal ion source. Samples were mounted onto silicon wafer pieces

using double-sided tape. Mass spectra were acquired in the negative and positive mode using Bi_3^{2+} primary ion clusters, accelerated at 25 keV. The target current during analysis was ~0.3 pA, with a 500 μm × 500 μm analysis area and a cycle time of 120 μs in interlaced mode. During all ToF-SIMS experiments, the analysis chamber pressure was 10^{-9} mbar or better, and the total ion dose was well below the static limit (10^{13} ions/cm^2).

Fabrication of Inks. The silicon and germanium alloy inks were made by sonicating the untreated nanoparticles in benzonitrile or acetonitrile for short times (10 min), medium-range times (4 h), or extended times (24 h) in a low-power ultrasonic bath (VWR model 150HT, 35 kHz). The water in the bath was changed frequently (*ca.* every 30 min) to prevent temperature rises in the water bath. The resulting dispersions were then filtered through 0.2 μm PTFE filters. The filtrate was collected as an ink and stored under nitrogen.

Acknowledgment. This study was supported by grants from the Ford Foundation, Collegiate Science and Technology Entry Program, the Chemistry and Life Sciences Division of the Air Force Office of Scientific Research, and the University at Buffalo Interdisciplinary Research and Creative Activities Fund. Jasmine May, Michelle Marchany, and Thao Nguyen are also acknowledged for assisting with experiments in this paper.

Supporting Information Available: TEM, TOF SIMS, SAED, pictures, and FTIR of etched nanoparticles. The material is available free of charge *via* the Internet at http://pubs.acs.org.

REFERENCES AND NOTES

1. Prasad, P. N. *Biophotonics*; Wiley-Interscience: Hoboken, NJ, 2003.
2. Prasad, P. N. *Nanophotonics*; Wiley-Interscience: Hoboken, NJ, 2004.
3. Yongping, D.; Ying, D.; Bapat, A.; Nowak, J. D.; Carter, C. B.; Kortshagen, U. R.; Campbell, S. A. Single Nanoparticle Semiconductor Devices. *IEEE T. Electron Dev.* **2006**, *53*, 2525–2531.
4. Sun, Q.; Wang, Y. A.; Li, L. S.; Wang, D.; Zhu, T.; Xu, J.; Yang, C.; Li, Y. Bright, Multicoloured Light-Emitting Diodes Based on Quantum Dots. *Nat. Photonics* **2007**, *1*, 717–722.
5. Gur, I.; Fromer, N. A.; Geier, M. L.; Alivisatos, A. P. Air-Stable All-Inorganic Nanocrystal Solar Cells Processed from Solution. *Science* **2005**, *310*, 462–465.
6. Wang, L. G.; Pennycook, S. J.; Pantelides, S. T. The Role of the Nanoscale in Surface Reactions: Co_2 on CdSe. *Phys. Rev. Lett.* **2002**, *89*, 075506.
7. Yong, K.-T.; Roy, I.; Swihart, M. T.; Prasad, P. N. Multifunctional Nanoparticles as Biocompatible Targeted Probes for Human Cancer Diagnosis and Therapy. *J Mater Chem* **2009**, *19*, 4655–4672.
8. Gao, X. H.; Cui, Y. Y.; Levenson, R. M.; Chung, L. W. K.; Nie, S. M. *In Vivo* Cancer Targeting and Imaging with Semiconductor Quantum Dots. *Nat. Biotechnol.* **2004**, *22*, 969–976.
9. Zimmer, J. P.; Kim, S.-W.; Ohnishi, S.; Tanaka, E.; Frangioni, J. V.; Bawendi, M. G. Size Series of Small Indium Arsenide−Zinc Selenide Core−Shell Nanocrystals and Their Application to in Vivo Imaging. *J. Am. Chem. Soc.* **2006**, *128*, 2526–2527.
10. Hua, F. J.; Swihart, M. T.; Ruckenstein, E. Efficient Surface Grafting of Luminescent Silicon Quantum Dots by Photoinitiated Hydrosilylation. *Langmuir* **2005**, *21*, 6054–6062.
11. Peter, L. M.; Riley, D. J.; Tull, E. J.; Wijayantha, K. G. U. Photosensitization of Nanocrystalline TiO_2 by Self-Assembled Layers of CdS Quantum Dots. *Chem. Commun.* **2002**, 1030–1031.
12. Robel, I.; Subramanian, V.; Kuno, M.; Kamat, P. V. Quantum Dot Solar Cells. Harvesting Light Energy with CdSe Nanocrystals Molecularly Linked to Mesoscopic TiO_2 Films. *J. Am. Chem. Soc.* **2006**, *128*, 2385–2393.
13. Erwin, S. C.; Zu, L.; Haftel, M. I.; Efros, A. L.; Kennedy, T. A.; Norris, D. J. Doping Semiconductor Nanocrystals. *Nature* **2005**, *436*, 91–94.
14. Pi, X. D.; Gresback, R.; Liptak, R. W.; Campbell, S. A.; Kortshagen, U. Doping Efficiency, Dopant Location, and Oxidation of Si Nanocrystals. *Appl. Phys. Lett.* **2008**, *92*, 259902.
15. Norris, D. J.; Efros, A. L.; Erwin, S. C. Doped Nanocrystals. *Science* **2008**, *319*, 1776–1779.
16. Swafford, L. A.; Weigand, L. A.; Bowers, M. J.; McBride, J. R.; Rapaport, J. L.; Watt, T. L.; Dixit, S. K.; Feldman, L. C.; Rosenthal, S. J. Homogeneously Alloyed CdS_xSe_{1-x} Nanocrystals: Synthesis, Characterization, and Composition/Size-Dependent Band Gap. *J. Am. Chem. Soc.* **2006**, *128*, 12299–12306.
17. Jang, E.; Jun, S.; Pu, L. High Quality CdSeS Nanocrystals Synthesized by Facile Single Injection Process and Their Electroluminescence. *Abstr. Pap. Am. Chem. Soc.* **2004**, *227*, 151–IEC.
18. Bailey, R. E.; Nie, S. Alloyed Semiconductor Quantum Dots: Tuning the Optical Properties without Changing the Particle Size. *J. Am. Chem. Soc.* **2003**, *125*, 7100–7106.
19. Bardeen, J.; Brattain, W. H. Physical Principles Involved in Transistor Action. *Phys. Rev.* **1949**, *75*, 1208.
20. Whall, T. E.; Parker, E. H. C. Silicon-Germanium Heterostructures—Advanced Materials and Devices for Silicon Technology. *J. Mater. Sci.- Mater. Electron.* **1995**, *6*, 249–264.
21. Kubby, J. A.; Boland, J. J. Scanning Tunneling Microscopy of Semiconductor Surfaces. *Surf. Sci. Rep* **1996**, *26*, 61–204.
22. Bardeen, J.; Brattain, W. H. The Transistor, a Semi-Conductor Triode. *Phys. Rev.* **1948**, *74*, 230.
23. Morse, M. Germanium on Silicon Approaches III-V Semiconductors in Performance. *Laser Focus World* **2007**, *43*, 111–113.
24. Precker, J. W.; da Silva, M. A. Experimental Estimation of the Band Gap in Silicon and Germanium from the Temperature-Voltage Curve of Diode Thermometers. *Am. J. Phys.* **2002**, *70*, 1150–1153.
25. Míguez, H.; Chomski, E.; García-Santamaría, F.; Ibisate, M.; John, S.; López, C.; Meseguer, F.; Mondia, J. P.; Ozin, G. A.; Toader, O.; Driel, H. M. v. Photonic Bandgap Engineering in Germanium Inverse Opals by Chemical Vapor Deposition. *Adv. Mater.* **2001**, *13*, 1634–1637.
26. Kartopu, G.; Bayliss, S. C.; Ekinci, Y.; Parker, E. H. C.; Naylor, T. Observation of Phonon Confinement in Sige Nanocrystals and Preferential Etching of Si in Porous $Si_{1-x}Ge_x$ Films. *Phys. Status Solidi A* **2003**, *197*, 263–268.
27. Takeoka, S.; Toshikiyo, K.; Fujii, M.; Hayashi, S.; Yamamoto, K. Photoluminescence from $Si_{1-x}Ge_x$ Alloy Nanocrystals. *Phys. Rev. B* **2000**, *61*, 15988.
28. Joshi, K. U.; Kabiraj, D.; Narsale, A. M.; Avasthi, D. K.; Gundurao, T. K.; Warang, T. N.; Kothari, D. C. Role of Rapid Thermal Annealing in the Formation of Crystalline SiGe Nanoparticles. *Surf. Coat. Technol.* **2009**, *203*, 2497–2500.
29. Kolobov, A.; Oyanagi, H.; Usami, N.; Tokumitsu, S.; Hattori, T.; Yamasaki, S.; Tanaka, K.; Ohtake, S.; Shiraki, Y. Raman Scattering and X-Ray Absorption Studies of Ge-Si Nanocrystallization. *Appl. Phys. Lett.* **2002**, *80*, 488–490.
30. Liao, Y. C.; Lin, S. Y.; Lee, S. C.; Chia, C. T. Spherical SiGe Quantum Dots Prepared by Thermal Evaporation. *Appl. Phys. Lett.* **2000**, *77*, 4328–4329.
31. Lin, C. W.; Lin, S. Y.; Lee, S. C.; Chia, C. T. Structural and Optical Properties of Silicon-Germanium Alloy Nanoparticles. *J. Appl. Phys.* **2002**, *91*, 2322–2325.
32. Schittenhelm, P.; Abstreiter, G.; Darhuber, A.; Bauer, G.; Werner, P.; Kosogov, A. Growth of Self-Assembled Homogeneous SiGe-Dots on Si(100). *Thin Solid Films* **1997**, *294*, 291–295.
33. Tang, Y. S.; Sotomayor Torres, C. M.; Ni, W. X.; Hansson, G. V. Room Temperature Electroluminescence of Nanofabricated Si-$Si_{1-x}Ge_x$ Quantum Dot Diodes. *Superlattice Microstruct.* **1996**, *20*, 505–511.
34. Gresback, R.; Holman, Z.; Kortshagen, U. Nonthermal Plasma Synthesis of Size-Controlled, Monodisperse, Freestanding Germanium Nanocrystals. *Appl. Phys. Lett.* **2007**, *91*, 093119.
35. Lew, K.-K.; Pan, L.; Dickey, E. C.; Redwing, J. M. Vapor-Liquid-Solid Growth of Silicon-Germanium Nanowires. *Adv. Mater.* **2003**, *15*, 2073–2076.

36. Wu, Y.; Fan, R.; Yang, P. Block-by-Block Growth of Single-Crystalline Si/SiGe Superlattice Nanowires. *Nano Lett.* **2002**, *2*, 83–86.
37. Pi, X. D.; Kortshagen, U. Nonthermal Plasma Synthesized Freestanding Silicon-Germanium Alloy Nanocrystals. *Nanotechnology* **2009**, *20*, 295602.
38. Bapat, A.; Perrey, C. R.; Campbell, S. A.; Carter, C. B.; Kortshagen, U. Synthesis of Highly Oriented, Single-Crystal Silicon Nanoparticles in a Low-Pressure, Inductively Coupled Plasma. *J. Appl. Phys.* **2003**, *94*, 1969–1974.
39. Cannon, W. R.; Danforth, S. C.; Flint, J. H.; Haggerty, J. S.; Marra, R. A. Sinterable Ceramic Powders from Laser-Driven Reactions: I, Process Description and Modeling. *J. Am. Ceram. Soc.* **1982**, *65*, 324–330.
40. Cannon, W. R.; Danforth, S. C.; Haggerty, J. S.; Marra, R. A. Sinterable Ceramic Powders from Laser-Driven Reactions: II, Powder Characteristics and Process Variables. *J. Am. Ceram. Soc.* **1982**, *65*, 330–335.
41. Ma, L. B.; Schmidt, T.; Guillois, O.; Huisken, F. Evolution of Photoluminescence Properties of $Si_{1-x}Ge_x$ Nanocrystals Synthesized by Laser-Induced Pyrolysis. *Appl. Phys. Lett.* **2009**, *95*, 013115.
42. Holman, Z. C.; Kortshagen, U. R. Nanocrystal Inks without Ligands: Stable Colloids of Bare Germanium Nanocrystals. *Nano Lett.* **2011**, *11*, 2133–2136.
43. Lutterotti, L. Total Pattern Fitting for the Combined Size-Strain-Stress-Texture Determination in Thin Film Diffraction. *Nucl. Instrum. Methods B* **2010**, *268*, 334–340.
44. Kasper, E.; Lyutovich, K. *Properties of Silicon Germanium and SiGe:Carbon*. Institution of Engineering and Technology, Edison: New Jersey, 2000; pp 45−47.
45. Yang, Y. M.; Wu, X. L.; Yang, L. W.; Kong, F. Twinning Defects in Spherical GeSi Alloy Nanocrystals. *J. Cryst. Growth* **2006**, *291*, 358–362.
46. Li, X.; He, Y.; Talukdar, S. S.; Swihart, M. T. Process for Preparing Macroscopic Quantities of Brightly Photoluminescent Silicon Nanoparticles with Emission Spanning the Visible Spectrum. *Langmuir* **2003**, *19*, 8490–8496.